Research Square

Preprints are preliminary reports that have not undergone peer review.
They should not be considered conclusive, used to inform clinical practice,
or referenced by the media as validated information.

Engineering Hybrid Fano Resonances in Periodic Gold Nanorod– Dye Architectures for High-Performance Refractive-Index Sensing

maedeh sadaghzadeh
Persian Gulf University
Ahmad Mohammadi
mohammadi@pgu.ac.ir

Persian Gulf University
tahmineh jalali
Persian Gulf University

Research Article

Keywords: Fano resonance, plasmonic sensing, gold nanorods, plasmon–exciton interaction, refractive-index sensing, 3D-FDTD, label-free detection

Posted Date: July 22nd, 2026

DOI: https://doi.org/10.21203/rs.3.rs-10395004/v1

License: This work is licensed under a Creative Commons Attribution 4.0 International License.
Read Full License

Additional Declarations: No competing interests reported.

Engineering Hybrid Fano Resonances in Periodic Gold Nanorod–Dye Architectures for High-Performance Refractive-Index Sensing

Maedeh Sadeghzadeh, Ahmad Mohammadi*, Tahmineh Jalali *
Physics Department, Persian Gulf University,
Bushehr7516913817, Iran
Tel: +98-771-334-54408 *E-mail: mohammadi@pgu.ac.ir, jalali@pgu.ac.ir

Abstract

A hybrid plasmon–exciton nanostructure consisting of periodic gold nanorods conformally coated with a molecular dye layer is theoretically investigated as a high-performance refractive-index sensor. Three-dimensional finite-difference time-domain (3D-FDTD) simulations demonstrate that cooperative interaction among localized surface plasmon resonances (LSPRs), molecular excitons, and Fabry–Pérot cavity feedback produces a narrow Fano-like reflection resonance with a linewidth of 2.87 nm and a quality factor of $Q \approx 343$. The resonance behavior was systematically investigated by varying the nanorod height, dye-layer thickness, and lattice period. Building on this parametric analysis, the study establishes a resonance-engineering framework in which cooperative plasmon–exciton coupling, lattice-assisted optical confinement, and Fabry–Pérot cavity feedback are intentionally combined to generate narrow hybrid Fano resonances with improved spectral selectivity and sensing performance. The selected configuration, comprising a 25 nm nanorod height, 30 nm dye layer, and 620 nm lattice period, achieves a maximum wavelength sensitivity of 333.93 nm RIU^{-1} with a figure of merit of 116.35 RIU^{-1} and an estimated detection limit of 3.0×10^{-5} RIU for biomaterial sensing in the refractive-index range of 1.46–1.55. For low-index gaseous environments, the same platform enables fixed-wavelength intensity interrogation with an intensity sensitivity of 17.58 RIU^{-1}. The enhanced performance is attributed to strong electromagnetic field localization, efficient overlap between the hybrid optical mode and the surrounding analyte, and collective lattice effects. The proposed architecture supports both wavelength-shift and intensity-based sensing within a single platform and provides general design principles for engineering hybrid Fano resonances in compact, label-free plasmonic sensors for biochemical and environmental monitoring.\.

Keywords: Fano resonance; plasmonic sensing; gold nanorods; plasmon–exciton interaction; refractive-index sensing; 3D-FDTD; label-free detection.

1. Introduction

Sensors play a central role in medicine, industry, and environmental monitoring. Among them, biosensors are analytical devices that detect biological or chemical species by converting molecular interactions into measurable signals [1-4]. A typical biosensor includes a bioreceptor (e.g., enzyme, antibody, nucleic acid), a transducer (e.g., nanomaterials), and an electronic system for signal processing and readout [5-8]. Among optical biosensing technologies, surface plasmon resonance (SPR) is a widely used label-free technique that enables real-time monitoring of molecular interactions with high sensitivity and rapid response [5-10]. By eliminating the need for molecular labeling, SPR reduces both assay complexity and possible perturbation of binding events [1]. SPR biosensors have therefore been widely applied to the analysis of biomolecular interactions, including protein binding and DNA hybridization. Their operation relies on the resonant excitation of collective electron oscillations at a metal–dielectric interface under appropriate optical conditions [11-13]. Plasmonic waveguide platforms, especially metal–dielectric–metal (MDM) structures, are of considerable interest for refractive-index (RI) sensing because they support deeply subwavelength optical confinement across a broad spectral range and are relatively straightforward to fabricate [14-16]. As a result, MDM-based plasmonic sensors have been widely investigated in a variety of resonant configurations, including circular ring resonators, square ring resonators, split-ring structures, notched resonators, gear-shaped nanocavities, and hexagonal cavities [9, 10, 14-17]. In parallel, slow-light effects in nanophotonic systems have attracted attention because they increase the local optical energy density and thereby enhance light–matter interaction, which is beneficial for sensing at the nanoscale [18]. Therefore, it is essential to investigate the sensing characteristics of plasmonic MDM waveguide-based slow-light RI sensors. This sensing approach enables identification of the target substance without the use of labeling reagents. These properties make plasmonic MDM waveguide systems attractive candidates for compact and high-performance RI sensors [17-19]. More broadly, optical sensing platforms have been developed using several techniques, including fluorescence, phosphorescence, Raman spectroscopy, interferometry, guided-mode spectroscopy, and surface plasmon resonance[19-23]. Among these approaches, plasmonic sensing at the nanoscale is particularly effective because metallic nanostructures can generate highly localized electromagnetic fields, thereby enhancing interactions with nearby analytes [20]. The product of this reaction can be a chemical, optical, or electrical message [21]. Different types of optical methods for the development of chemical and biological sensors include spectroscopy (fluorescence, phosphorescence, and Raman), interferometry, spectroscopy of guided modes in optical waveguide structures (coupling with grating and resonance with a mirror), and resonance of surface plasmons[22-24].

Plasmonic modes are generally categorized into surface plasmon polaritons (SPPs) and localized surface plasmons (LSPs). SPPs are propagating waves bound to the metal–dielectric interface, exhibiting exponential decay in both media and high sensitivity to environmental refractive index change. In contrast, LSPs occur in metal nanoparticles, where collective electron oscillations resonate with incident light and generate intense local fields. The resonance behavior depends on

nanoparticle size, shape, composition, and surrounding dielectric properties [25-27]. Accordingly, in plasmonic nanosensors, the localized surface plasmon resonance is strongly influenced by nanoparticle geometry and by changes in the refractive index of the surrounding medium [7, 28]. The rapid development of nanostructured plasmonic sensors has significantly advanced analytical chemistry and label-free detection technologies [29, 30]. Because their optical response is highly sensitive to changes in the local dielectric environment, plasmonic nanostructures are well suited for detecting variations induced by refractive index, pH, temperature, and molecular binding events [31]. Such sensors have been applied to the detection of a broad range of targets, including small molecules, peptides, proteins, cells, and viruses [32, 33]. Plasmonic nanostructures provide a powerful sensing platform by converting subtle physicochemical changes near their surface into measurable shifts in optical signals [34-36]. Their strong light–matter interaction and tunable resonance behavior make them particularly effective for real-time, label-free monitoring of environmental changes and biomolecular interactions [37-40]. Their ability to monitor refractive-index changes in real time makes them highly valuable in biomedical diagnostics, environmental monitoring, and food safety [39, 41, 42]. In addition, plasmonic materials and device concepts have been extended from the visible into the infrared regime, thereby broadening the accessible sensing window and enabling multifunctional sensor platforms [34, 43]. For example, infrared SPR systems have shown strong potential for the selective and sensitive detection of small molecules, biomolecules, and even cancer cells [44, 45] [46].

Recent progress has also highlighted the importance of integrating plasmonic nanostructures with microfluidic platforms for real-time and label-free sensing in compact lab-on-a-chip devices [47, 48]. Xu et al. demonstrated that microfluidic systems incorporating plasmonic nanostructures can enhance fluorescence immunoassays while improving sensitivity and multiplexing capability [49] [50]. More broadly, the convergence of nanoplasmonics and microfluidics has accelerated advances in nanostructure fabrication, subwavelength fluid manipulation, and portable diagnostic systems [51] [52]. Despite these advances, conventional plasmonic refractive-index sensors often suffer from radiative and Ohmic losses, relatively broad resonance linewidths, and limited spectral selectivity, which restrict their sensitivity and practical performance. Consequently, there remains a need for sensing platforms capable of simultaneously achieving strong electromagnetic field confinement, narrow spectral resonances, tunable optical responses, and compatibility with integrated photonic and microfluidic systems. Although plasmon–exciton hybrid structures have been investigated in various nanophotonic configurations, the systematic engineering of Fano-like resonances in periodic gold nanorod–dye hybrid architectures for refractive-index sensing has received little attention. In this work, we present a design strategy that combines localized surface plasmon resonances, molecular excitonic transitions, lattice-assisted optical confinement, and cavity-mediated feedback to generate high-quality hybrid Fano resonances. Through systematic structural optimization, the proposed architecture supports both wavelength-shift and intensity-based interrogation within a single sensing platform, providing enhanced spectral selectivity, strong near-field localization, and improved refractive-index sensitivity. This work therefore

establishes practical design guidelines for engineering hybrid plasmon–exciton resonances in high-performance plasmonic sensors.

To address these limitations, this work introduces a periodic Au nanorod–dye hybrid architecture that intentionally exploits cooperative plasmon–exciton coupling, lattice-mediated optical confinement, and Fabry–Pérot cavity feedback to engineer narrow hybrid Fano resonances. Using 3D-FDTD simulations, we systematically investigate how these interacting mechanisms govern resonance formation, field localization, and sensing performance. Rather than focusing solely on parameter improvement, this study establishes a physics-based resonance-engineering framework for designing hybrid plasmonic sensors with improved spectral selectivity and refractive-index sensitivity.

2. Theoretical and Computational Aspects

2.1. Physical Principles of Hybrid Optical Modes

The sensing performance of the proposed nanostructure arises from the interaction among localized plasmonic resonances, excitonic absorption in the dye coating, and photonic feedback supported by the multilayer configuration. When gold nanorods are periodically arranged above a dielectric spacer and metallic back-reflector and coated with a molecular dye, multiple optical pathways coexist within the same spectral window and can interfere coherently, producing narrow spectral features suitable for refractive-index sensing.

2.1.1. Plasmonic Resonances and Exciton Coupling

The dominant plasmonic contribution originates from the LSPR supported by the gold nanorods. For the geometry considered here (diameter ≈ 20 nm, height ≈ 50 nm), the LSPR occurs in the visible to near-infrared region and generates strong near-field enhancement at the nanorod extremities. Introducing an excitonic dye layer adds a narrowband dispersive response that can spectrally overlap with the plasmonic resonance. The interaction between the plasmonic continuum and the excitonic transition results in hybridized (plexcitonic) modes and an asymmetric Fano-like reflection profile. The steep spectral slope of this Fano feature enables small refractive-index variations to produce measurable resonance shifts.

2.1.2. Photonic and Cavity Feedback Mechanisms

In addition to the LSPR–exciton interaction, the periodic nanorod array introduces lattice-mediated photonic effects. The array can act as a diffraction grating, where the mth-order diffraction angle, θ_m, is governed by:

$$sin\,\theta_m = sin\,\theta_i + m\frac{\lambda}{p} \qquad m = 1,2,3,\ldots$$

According to the relation, p, θ_m, θ_i , m, and λ are the periodicity of nanorods, the angle of scattered light, the angle of incident light, the order of diffraction, and the wavelength of light, respectively. These lattice effects can couple incident light to guided or leaky modes in the dye/dielectric region, introducing narrowband spectral contributions that interfere with the broader plasmonic response. Furthermore, the high-index layer and gold back-reflector form a Fabry–Perot–like cavity. Under approximate resonance conditions, $d = m\frac{\lambda}{2n}$, constructive interference enhances the optical field

within the active region, increasing the effective interaction length and potentially narrowing the resonance linewidth.

The combined action of (i) LSPR excitation, (ii) lattice-mediated photonic modes, and (iii) Fabry–Perot feedback produces a multi-channel interference process that yields a sharp Fano-like reflection response (Fig. 1). Strong plasmon–exciton coupling reduces radiative damping and sharpens the spectral profile, thereby increasing sensitivity to changes in the surrounding refractive index n.

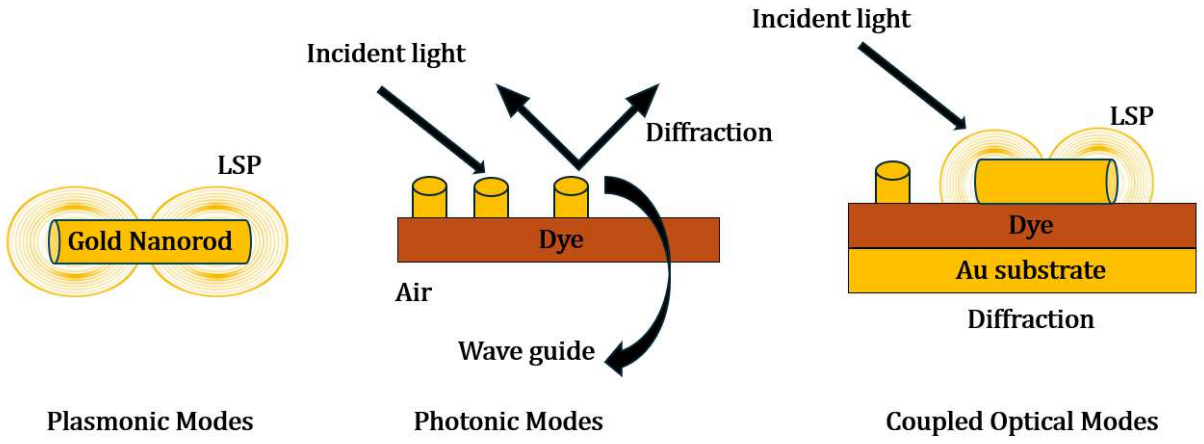


Fig. 1. Schematic of the dominant optical modes in the nanorod–dye sensor: (a) LSPR of Au nanorods, (b) photonic guided/leaky modes and grating diffraction in the dye layer, and (c) their coupled response in the full stack, assisted by Fabry–Perot-like feedback from the Au back-reflector, yielding a Fano-like sensing signature.

2.2. Numerical Simulation Strategy

2.2.1. 3D-FDTD Implementation

The optical response of the proposed structure was simulated using the 3D-FDTD method implemented in Lumerical FDTD Solutions. The computational domain, shown in Fig. 2, employed perfectly matched layers (PMLs) along the z direction to suppress artificial reflections, while periodic boundary conditions (PBCs) were applied along the x- and y-directions to represent an infinite periodic array. A transverse electric (TE)-polarized plane wave was launched normal to the structure. To resolve the strong field gradients near the metal–dielectric interface, a nonuniform conformal mesh was used, with a minimum mesh size of 6 nm in the nanorod/dye region. Reflection spectra were recorded using a frequency-domain monitor positioned above the structure.

The dispersive optical properties of the materials were incorporated through standard analytical models. The permittivity of gold was described using the Drude model:

$$\varepsilon(\omega) = \varepsilon_{\infty} - \frac{\omega_p^2}{\omega^2 + i\gamma\omega} \quad (1)$$

Where ω_p, ω, and γ are plasma frequency, incidence light frequency, and oscillating damping coefficient, respectively. The excitonic response of the dye layer was incorporated using the Lorentz model:

$$\varepsilon(\omega) = \varepsilon_\infty - \frac{f\omega_0^2}{\omega_0^2 - \omega^2 + i\gamma\omega} \quad (2)$$

Where ε, f, ω_0, and γ are the permeability coefficient of the surrounding environment, the power of the oscillator, the frequency of the molecule, and the damping coefficient. By integrating these models into the FDTD framework, we accurately simulated the complex electromagnetic behavior of hybrid metal–dye systems, as is depicted in Fig. 3. This dual-model approach allows for the precise simulation of the coherent interference that generates the Fano resonance.

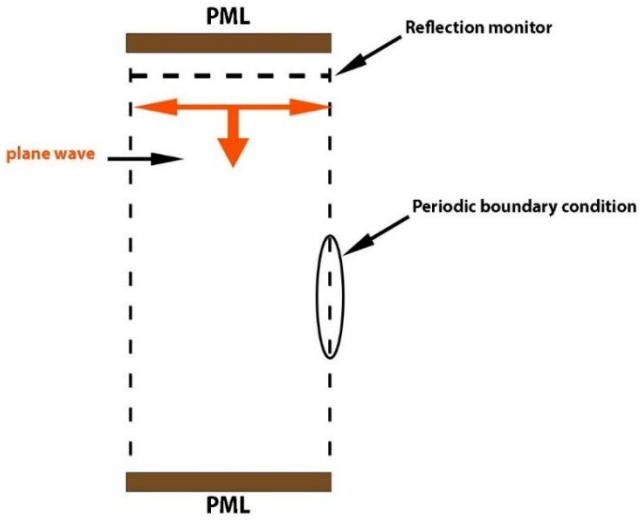


Fig. 2. The simulation space of the structure

2.2.2 Model Configuration and Simulation Setup

The simulated unit cell consists of cylindrical gold nanorods with diameter 20 nm and height 50 nm, positioned on a high-index silicon layer of thickness 100 nm (n=3.5), which is supported by a gold substrate of thickness 100 nm. Each nanorod is coated with a dye layer of thickness 30 nm. The structure was illuminated along the z-direction by a TE-polarized plane wave over the wavelength range 700–1200 nm. Reflection spectra were obtained using a monitor plane above the structure. To evaluate refractive-index sensing performance, the surrounding refractive index was varied to represent both biomaterial and gaseous analyte regimes, as summarized in Table S1. The principal geometrical and numerical parameters are listed in Tables 1 and 2.

Table 1. Simulation Setup: Boundary Conditions and Geometrical Parameters

Boundary Conditions	Z-direction (top & bottom): Absorbing boundary conditions using perfectly matched layers (PML) X and Y directions: Periodic boundary conditions
	Substrate: Gold, thickness = 100 nm

Geometrical Configuration	Dye coating: Thickness = 30 nm Nanorod (cylindrical): Height = 50 nm

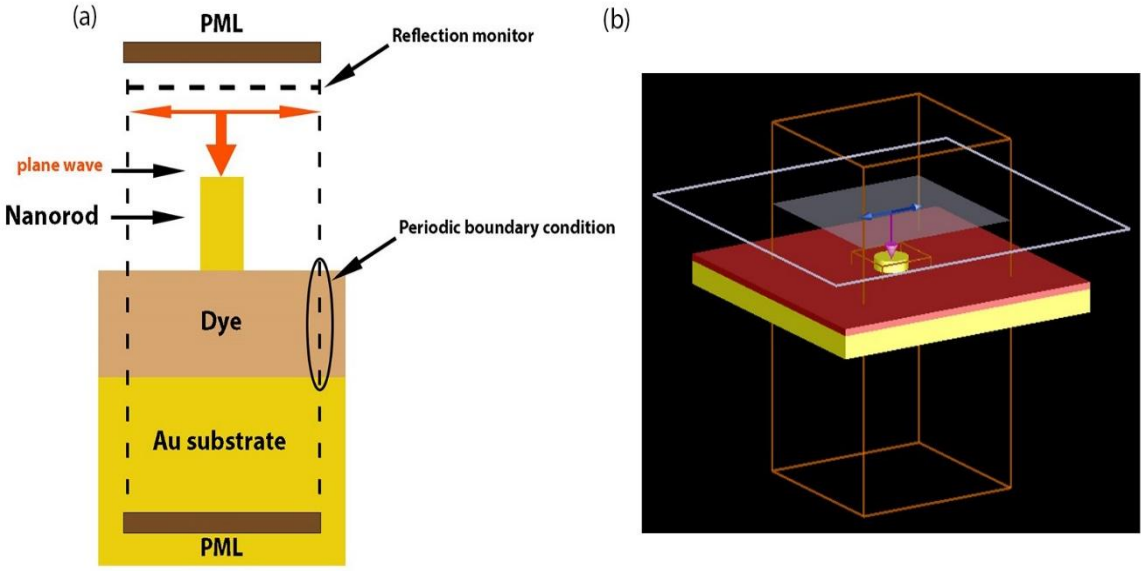


Fig. 3. a) A schematic of the three-dimensional space of the proposed structure. b) Simulation space to calculate the reflection of the nanorod on top of the structure.

Table 2: parameters of gold and dye in the Drude and Lorentz models

Material	**Model**	ε_p	$\omega_p\left(rad/_s\right)$	$\gamma_p\left(rad/_s\right)$	ε	f	$\gamma\left(rad/_s\right)$
Gold	Drude	9.5	$1.38504e+16$	$4.0007e+13$		———	
Dye	Lorentz		———		1.69	0.05	$4.2002e+12$

2.2.3. Sensing Evaluation Metrics

The sensing performance of the proposed hybrid plasmon–exciton structure was evaluated using both wavelength-shift and fixed-wavelength intensity interrogation. Wavelength interrogation tracks the resonance shift induced by variations in the surrounding refractive index, whereas intensity interrogation monitors the reflectance change at a selected wavelength on the steep slope of the Fano resonance. The latter is particularly suitable for gaseous sensing, where refractive-index variations are typically in the range of 10^{-6} to 10^{-4} RIU and the associated spectral shifts are often below the resolution of conventional spectrometers. The wavelength sensitivity is defined as:

$$S_\lambda = \frac{\Delta\lambda_{res}}{\Delta n} = \frac{\lambda_2 - \lambda_1}{n_2 - n_1} \quad (3)$$

where λ_1 and λ_2 represent the resonance wavelengths corresponding to refractive indices n_1 and n_2, respectively. S_λ was obtained from the slope of the linear regression of the resonance wavelength as a function of refractive index. The resonance linewidth was quantified by the full width at half maximum (FWHM). For a dip-type resonance, the half-depth reflectance is given by:

$$R_{1/2} = R_{min} + \frac{R_{base} - R_{min}}{2} \quad (4)$$

where R_{min} is the minimum reflectance at the resonance wavelength and R_{base} is the local baseline reflectance evaluated from the neighboring spectral region. The linewidth is then calculated as:

$$FWHM = |\lambda_L - \lambda_R| \quad (5)$$

where λ_L, and λ_R denote the left and right half-depth crossing wavelengths. The sensing figure of merit (FOM), which combines resonance sensitivity and linewidth, is defined as:

$$FOM = \frac{S_\lambda}{FWHM} \quad (6)$$

where a larger FOM indicates higher spectral resolution for refractive-index sensing. For fixed-wavelength interrogation, the intensity ratio is defined as:

$$R = \frac{I_{peak}}{I_{dip}} \quad (7)$$

where I_{peak}, and I_{dip} denote the reflectance at the Fano resonance peak and the deeper resonance dip, respectively. The corresponding intensity sensitivity is:

$$S_I = \frac{dR}{dn} = \frac{R_2 - R_1}{n_2 - n_1} \quad (8)$$

Where R_1 and R_2 are are the intensity ratios measured at refractive indices n_1 and n_2. In this study, S_I was determined from the slope of the linear regression of R versus n. For gaseous sensing, the normalized intensity variation was additionally evaluated as:

$$\frac{\Delta R}{R_0} = \frac{R(n) - R(n_0)}{R(n_0)} \quad (9)$$

Where n_0 is the refractive index of the reference medium.

2.2.3.1. Detection Limit

The detection limit (DL) represents the minimum detectable refractive-index variation. For wavelength interrogation:

$$DL_\lambda = \frac{\Delta\lambda_{min}}{S_\lambda} \quad (10)$$

Where $\Delta\lambda_{min}$ is the minimum resolvable wavelength shift of the measurement system. For intensity interrogation, $\Delta\lambda_{min} \approx 0.01$ nm. DL_λ is reported in RIU.

$$DL_I = \frac{\Delta R_{min}}{S_I} \quad (11)$$

Where ΔR_{min} is the minimum detectable intensity variation determined by the detector noise level. The visibility of the Fano resonance was quantified using the contrast ratio:

$$C = \frac{I_{peak} - I_{dip}}{I_{peak} + I_{dip}} \quad (12)$$

which provides a convenient measure of resonance modulation depth for comparing different structural configurations. The reflection spectra were fitted using the standard Fano line-shape model [28]:

$$R(\lambda) = R_b + R_0 \frac{(q+\epsilon)^2}{1+\epsilon^2}, \qquad \epsilon = \frac{2(\lambda-\lambda_0)}{\Delta\lambda} \tag{13}$$

Where R_b is the background reflectance, R_0 is the amplitude, q is the Fano asymmetry parameter, λ_0 is the resonance wavelength, and $\Delta\lambda$ is the linewidth parameter. The fitted value of q was used to quantify the asymmetry of the hybrid resonance. Similar formulations have been widely adopted for the analysis of plasmonic Fano resonances[53]. To relate electromagnetic confinement to sensing performance, first-order perturbation theory was employed. The resonance shift induced by a refractive-index perturbation is proportional to the fraction of electromagnetic energy confined within the analyte region [58]:

$$\Delta\lambda \propto \frac{\int_{analyte}[E]^2 dV}{\int_{total}[E]^2 dV} \Delta n \tag{14}$$

The confinement factor Γ is defined:

$$\Gamma = \frac{\int_{analyte}[E]^2 dV}{\int_{total}[E]^2 dV} \tag{15}$$

A larger Γ indicates stronger overlap between the localized optical field and the sensing medium, leading to greater refractive-index sensitivity. This parameter is subsequently used in Section 3 to correlate field localization with the measured sensing performance.

The fundamental physical mechanism governing the refractive-index sensitivity of our hybrid nanostructure is visualized in Fig. 4. By detailing the causal evolution from local dielectric perturbation to the formation of a hybrid Fano mode, this schematic highlights the multi-modal interaction—involving plasmonic, excitonic, and lattice/cavity feedback—that underpins the high sensitivity observed throughout our numerical simulations.

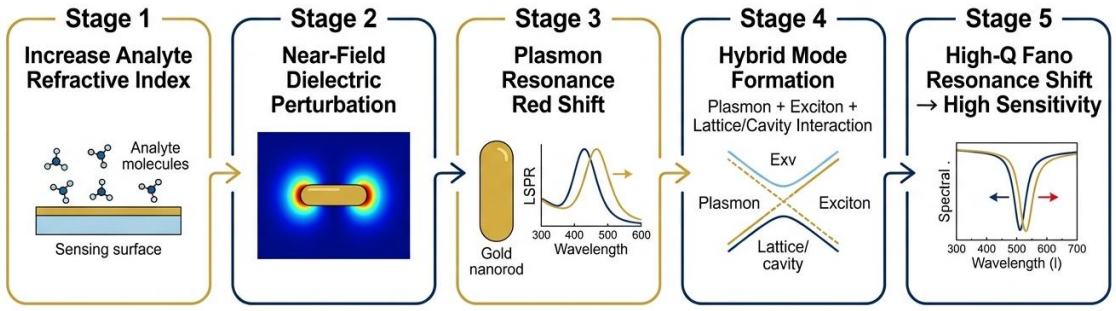


Fig. 4. Physical transduction mechanism of refractive-index sensing in the proposed hybrid plasmon–exciton nanostructure. An increase in the analyte refractive index perturbs the near-field dielectric environment, inducing a red shift of the LSPR. The displaced plasmonic mode interacts with the excitonic response of the molecular dye together with lattice-assisted and cavity-mediated optical effects, forming a hybrid Fano resonance. Owing to its narrow linewidth and strong spectral dispersion, small refractive-index variations produce pronounced spectral shifts, enabling high-sensitivity detection.

3. Results and Discussion

To establish the physical mechanism underlying the proposed sensing platform, we investigate how an excitonic overlayer modifies the plasmonic response of a periodic Au nanorod array through cooperative plasmon–exciton coupling. Rather than focusing solely on geometric optimization, this work establishes a resonance-engineering framework by identifying the cooperative roles of plasmon–exciton coupling, lattice-assisted optical confinement, and cavity feedback in the formation of narrow hybrid Fano resonances and their impact on refractive-index sensing. The unit-cell geometry, material models, and excitation/monitoring conditions are shown in Fig. 3. The discussion first examines the spectral signatures of the hybrid modes and then relates these signatures to the electromagnetic field localization responsible for the enhanced sensing performance.

3.1. Physical Origin of the Hybrid Fano Resonance

The physical origin of the hybrid Fano resonance can be understood from the reflection spectra of the periodic Au nanorod–dye architecture shown in Fig. 5. The spectra exhibit a characteristic Fano-like line shape consisting of a central reflection peak accompanied by two adjacent dips, which differs markedly from the symmetric Lorentzian response typically observed for isolated LSPRs.

The asymmetric spectral profile originates from the interference between a broad plasmonic resonance and a narrow excitonic resonance supported by the molecular dye layer. In the proposed architecture, the Au nanorods provide a broadband LSPR response, while the dye coating introduces a spectrally narrower dispersive contribution. Their spectral overlap, together with optical feedback from the multilayer stack, produces a hybrid resonance with pronounced asymmetry and enhanced spectral selectivity.

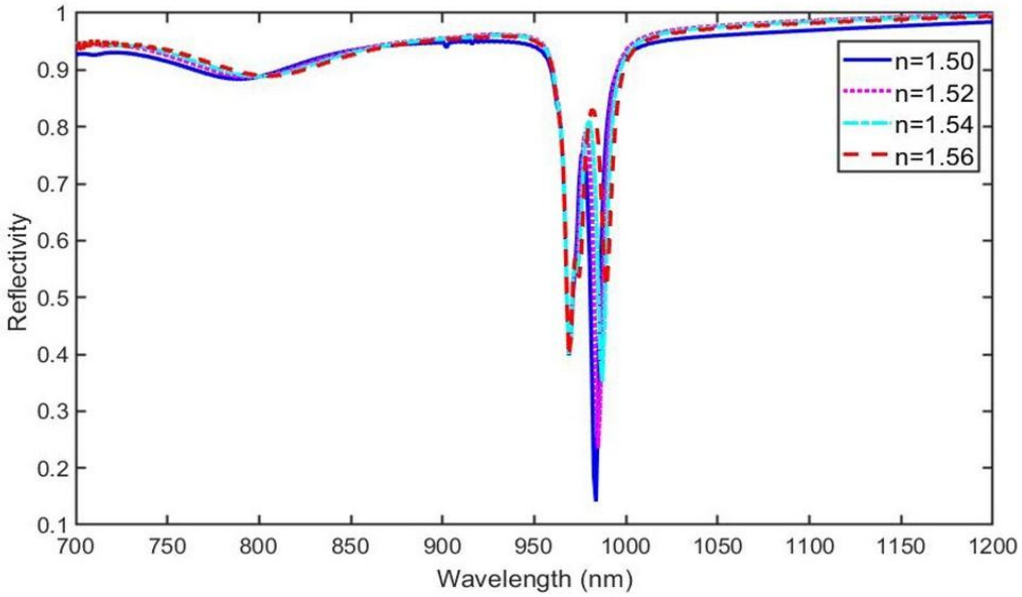


Fig. 5. Reflection spectra of the Au nanorod–dye hybrid structure for different surrounding refractive indices, showing the evolution of the Fano-like resonance induced by plasmon–exciton coupling.

Fitting the simulated spectrum with the standard Fano line-shape model yields an asymmetry parameter of $q \approx 1.2$, indicating a moderately asymmetric resonance. The extracted linewidth is FWHM ≈ 2.87 nm at a resonance wavelength near 976.7 nm, corresponding to a quality factor of $Q \approx 343$. Such a narrow linewidth is considerably smaller than that of many conventional LSPR sensors and is advantageous for resolving small refractive-index-induced spectral shifts. The emergence of the narrow Fano resonance originates from interference between the spectrally broad plasmonic mode supported by the Au nanorods and the spectrally narrow excitonic transition of the molecular dye. The periodic arrangement further introduces lattice-mediated optical coupling, which suppresses radiative losses and redistributes the electromagnetic field toward the nanorod–dye interface. This cooperative interaction increases the lifetime of the hybrid mode and results in a narrower resonance linewidth together with enhanced spectral asymmetry. To evaluate the sensing response, the surrounding refractive index was varied from 1.50 to 1.56. A clear and systematic redshift of the resonance dip is observed: the resonance wavelength shifts from 983.607 nm at n = 1.50 to 987.024 nm at n = 1.56. Linear regression of the resonance wavelength versus refractive index gives a wavelength sensitivity of $S_\lambda = 57.10$ nm/RIU with $R^2 = 0.999$, confirming the excellent linearity of the response in this range.

The corresponding FOM, calculated from the measured sensitivity and linewidth, is approximately 19.9 RIU^{-1}. The high FOM arises from the combination of a measurable resonance shift and a narrow spectral feature, enabling accurate determination of small refractive-index variations. Inclusive, the results demonstrate that the periodic nanorod–dye architecture supports a highly selective Fano-like resonance that is strongly responsive to changes in the local dielectric environment. This resonance forms the basis for the enhanced sensing performance analyzed in the following sections.

3.2. Electric-Field Localization and Hybrid Mode Formation

To clarify the physical origin of the Fano resonance and its contribution to refractive-index sensing, the spatial distributions of the electric-field intensity were analyzed at three characteristic wavelengths of the reflection spectrum: the first dip (968.858 nm), the central peak (976.744 nm), and the second dip (983.607 nm), as illustrated in Fig. 6. These field maps provide direct insight into how the hybrid optical mode evolves across the resonance.

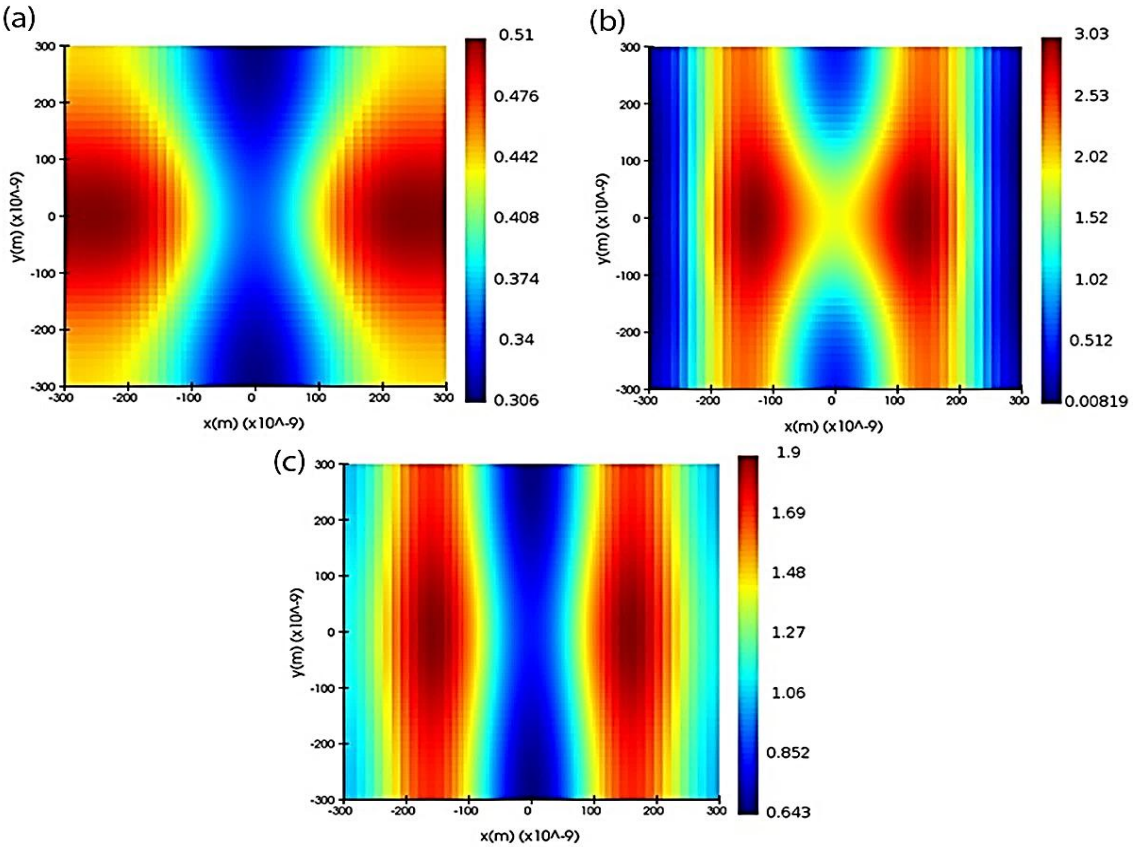


Fig. 6. Spatial distributions of electric-field intensity E^2 within the full hybrid structure at the three characteristic wavelengths of the Fano resonance: (a) 968.858 nm (first dip), (b) 976.744 nm (central peak), and (c) 983.607 nm (second dip). The central peak (b) exhibits maximum field build-up due to constructive interference, while the dips (a, c) result from destructive interference, leading to suppressed net intensity. Colorbar limits: (a) ~0.51, (b) ~3.03, (c) ~1.90 (arb. units).

3.2.1. Vertical Field Distributions: Cavity-Assisted Interference

The cross-sectional field distributions reveal distinct interference behaviors at the three spectral positions. At the resonance peak (976.744 nm), the electromagnetic field is strongly confined within the nanorod–dye region, whereas substantially weaker fields are observed at the two dip wavelengths. This behavior is consistent with constructive interference occurring near the resonance peak, while destructive interference suppresses the optical field at the neighboring spectral dips. The field enhancement extends throughout the dye-coated nanorods and partially into the surrounding dielectric environment, indicating efficient overlap between the localized electromagnetic field and the sensing region. Such overlap is essential for refractive-index sensing because perturbations in the surrounding dielectric medium directly influence the effective optical mode. The observed standing-wave pattern across the multilayer structure further suggests that the dielectric spacer and metallic reflector provide additional optical feedback, reinforcing the localized plasmonic response and contributing to the formation of the narrow Fano-like resonance. [50–52].

3.2.2. Field Localization on the Nanorod Surface

Fig. 7 presents the surface electric-field distributions on the Au nanorods at the same three wavelengths. At both resonance dips, the electromagnetic field is primarily concentrated near the nanorod ends, exhibiting the characteristic tip enhancement associated with localized surface plasmon resonances. The corresponding maximum field enhancements are approximately $|E|^2/|E_0|^2 \approx 21.6$ and 51.6, respectively.

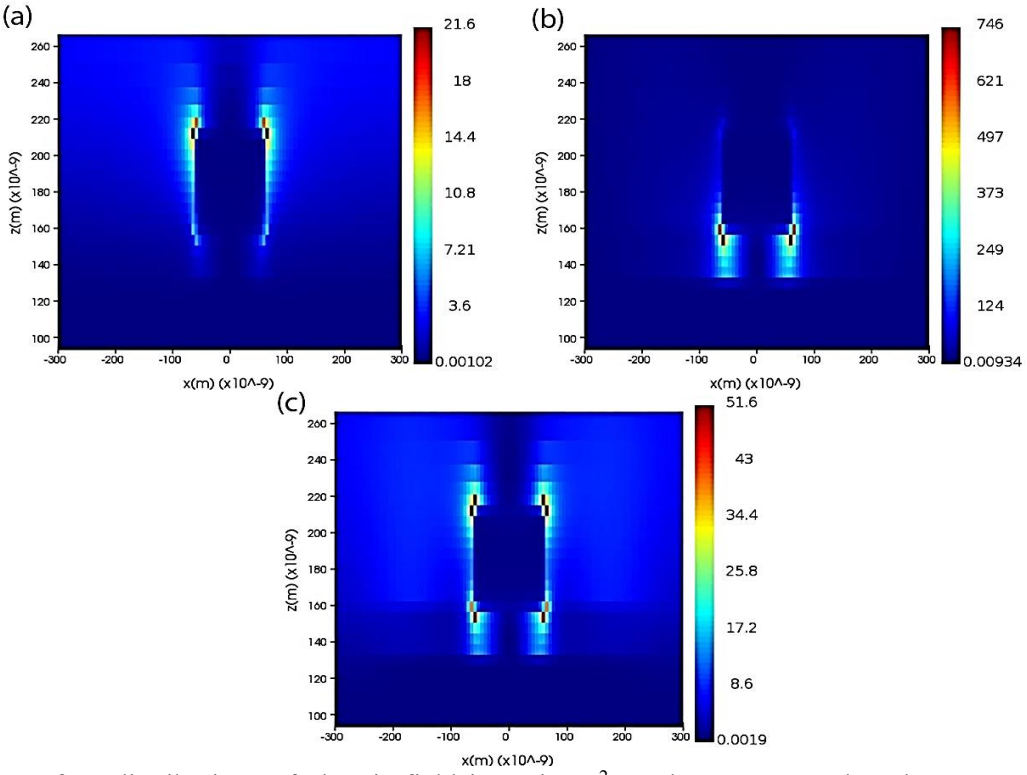


Fig. 7. Surface distributions of electric-field intensity E^2 on the Au nanorod at the Fano resonance features: (a) 968.858 nm (first dip), (b) 976.744 nm (central peak), and (c) 983.607 nm (second dip). Maximum surface localization and field enhancement occur at the central peak (b), indicating optimal plasmon–exciton hybridization and maximum overlap with the analyte near the metal–dye interface. Colorbar limits: (a) ~21.6, (b) ~746, (c) ~51.6 (arb. units).

In contrast, the central resonance peak exhibits dramatically stronger field localization, reaching a maximum enhancement of approximately $|E|^2/|E_0|^2 \approx 746$. Unlike the dip wavelengths, the enhanced field is distributed not only at the nanorod tips but also along the nanorod sidewalls and the metal–dye interface, thereby increasing the interaction volume between the optical mode and the surrounding analyte. This stronger electromagnetic overlap makes the hybrid resonance more sensitive to refractive-index perturbations. According to first-order perturbation theory, the resonance shift is proportional to the fraction of the electromagnetic energy confined within the sensing region; therefore, increased field localization directly enhances the wavelength sensitivity. This interpretation is consistent with the confinement-factor analysis presented in Section 2.2.3, where a larger fraction of the optical energy resides within the analyte volume. Overall, the field-

distribution analysis demonstrates that the enhanced sensing performance originates from the cooperative interaction of localized surface plasmons, plasmon–exciton coupling, lattice-assisted optical confinement, and cavity-enhanced optical feedback, which together maximize electromagnetic confinement within the sensing region [33–35].

3.3. Effect of Nanorod Height on Fano Resonance Characteristics

The nanorod height is one of the primary geometrical parameters governing the optical response of the proposed hybrid structure because it simultaneously influences the localized plasmon resonance, optical confinement, and interaction with the excitonic dye layer. To investigate its effect, the nanorod height was varied from 25 to 75 nm while maintaining a constant lattice period (p = 600 nm) and dye-layer thickness (t_{dye} = 30 nm), summarized in Table 3. The corresponding reflection spectra are presented in Fig. 8.

Table 3. Summary of the structural parameter study and the corresponding physical mechanisms governing the hybrid Fano resonance and sensing performance.

Parameter	Optimum	Physical Mechanism	Result
Nanorod height	25 nm	Reduced radiative damping and stronger near-field localization	Higher Q and lower FWHM
Dye thickness	30 nm	Strong plasmon–exciton mode overlap	Highest resonance contrast and sensitivity
Lattice period	620 nm	Improved lattice-assisted optical confinement	Maximum spectral selectivity
Combined parameter configuration	—	Cooperative interaction of all resonance-engineering mechanisms	Best sensing performance

3.3.1. Spectral Evolution

As shown in Fig. 8, the structure with h = 25 nm exhibits the sharpest and most pronounced Fano-like resonance, characterized by a narrow linewidth and high spectral contrast. Increasing the nanorod height progressively broadens the resonance while reducing the peak-to-dip contrast, indicating a gradual degradation of the spectral selectivity. The extracted resonance parameters are summarized in Table S2. The resonance linewidth increases from 2.87 nm for h = 25 nm to 4.52 nm and 7.38 nm for heights of 50 nm and 75 nm, respectively. Consequently, the quality factor decreases from approximately 340 to 134, while the contrast ratio is reduced from 0.62 to 0.28. In addition to the linewidth broadening, the secondary resonant features observed between 750 and 850 nm become progressively weaker for taller nanorods, indicating reduced spectral definition of the hybrid optical response. The complete numerical results from the structural parameter study, including all simulated parameter variations and the corresponding resonance characteristics, are provided in Table S4 of the Supplementary Information.

3.3.2. Physical Mechanisms

The observed spectral evolution reflects the influence of nanorod geometry on the balance between plasmonic confinement and radiative losses. For shorter nanorods, the localized plasmon resonance overlaps more effectively with the excitonic response of the dye layer, resulting in a

well-defined asymmetric Fano resonance with high spectral contrast. As the nanorod height increases, the resonance gradually broadens because the optical mode becomes less confined and radiative losses become more significant. These effects reduce the spectral selectivity of the hybrid resonance and consequently decrease the quality factor. The field distributions presented in Section 3.2 provide further physical evidence for the proposed resonance-engineering mechanism. The cooperative interaction between localized plasmons, molecular excitons, and lattice-assisted optical modes produces stronger electromagnetic confinement, increasing the overlap between the hybrid optical mode and the surrounding analyte. According to perturbation theory, this enhanced field–analyte interaction leads directly to larger resonance shifts and, consequently, higher refractive-index sensitivity.

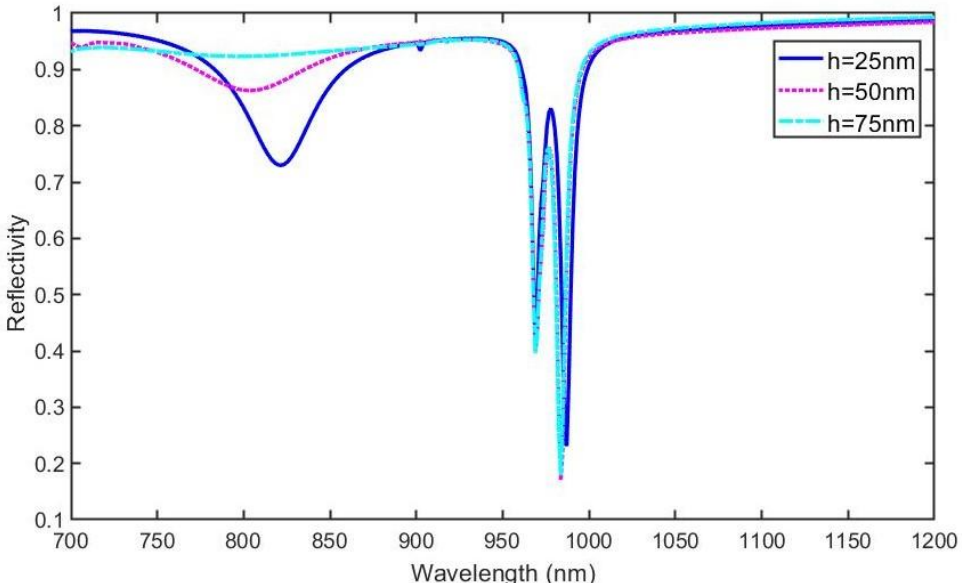


Fig. 8. Reflection spectra of the periodic nanorod–dye structure for a fixed lattice period of p=600nm and varying nanorod (grating) heights: h=25nm, 50 nm, and 75 nm. The smallest height (h=25 nm) produces the most distinct Fano-like feature (sharp peak between two dips) with higher spectral contrast, whereas increasing h progressively broadens the resonance and suppresses secondary features in the 750–850 nm range, consistent with increased radiative leakage and damping.

3.3.3. Implications for Refractive-Index Sensing

The spectral characteristics directly influence the sensing performance. Because the wavelength sensitivity depends not only on the resonance shift but also on the resonance linewidth, narrower resonances provide significantly larger FOM. Using the selected periodicity (p = 620 nm), the calculated FOM decreases from approximately 40 RIU^{-1} for h = 25 nm to 25 RIU^{-1} and 16 RIU^{-1} for nanorod heights of 50 nm and 75 nm, respectively. Similarly, the reduction in contrast ratio with increasing height limits the effectiveness of fixed-wavelength intensity interrogation by decreasing the available modulation depth. These results demonstrate that relatively short nanorods provide the most favorable balance between spectral linewidth, electromagnetic field localization, and sensing performance. For the present architecture, a nanorod height of

approximately 25 nm provides the most favorable resonance characteristics and was therefore selected for the subsequent parametric analysis. Increasing the nanorod height initially strengthens the localized surface plasmon resonance by increasing the effective oscillation volume of the conduction electrons, thereby enhancing near-field confinement. Beyond this value, however, radiative damping becomes increasingly significant, broadening the resonance and reducing the quality factor. Consequently, an intermediate nanorod height provides an effective balance between field confinement and radiation losses.

The effects of the principal structural parameters on the hybrid Fano resonance are summarized in Table 4. Rather than simply identifying a preferred geometry, the parametric study reveals the distinct physical role of each structural parameter in governing the resonance characteristics. Specifically, the nanorod height primarily controls radiative damping and near-field localization, the dye-layer thickness determines the strength of plasmon–exciton coupling, and the lattice period regulates lattice-assisted optical confinement. Their cooperative interaction gives rise to a narrow hybrid Fano resonance with enhanced spectral selectivity, high quality factor, and improved refractive-index sensing performance. These findings establish practical resonance-engineering guidelines for the design of high-performance hybrid plasmonic sensors.

3.4. Structural Parameters and Refractive Index Sensor performance

Following optimization of the nanorod height, the sensing characteristics of the proposed hybrid platform were further investigated by examining the influence of two additional structural parameters: the molecular dye-layer thickness and the lattice periodicity. These parameters determine the spectral overlap between the plasmonic and excitonic resonances, the optical confinement, and the interaction of the hybrid mode with the surrounding dielectric environment.

3.4.1. Effect of Dye-Layer Thickness

The thickness of the excitonic dye layer influences both the optical path length and the strength of the interaction between the molecular excitons and the localized plasmonic field. To evaluate this effect, the dye thickness was varied from 30 to 90 nm while maintaining a fixed nanorod height (25 nm) and lattice period (600 nm). As shown in Fig. 9, increasing the dye thickness produces a gradual redshift of the hybrid resonance. The resonance wavelength moves from 983.6 nm for a 30 nm dye layer to approximately 997.8 nm for a 90 nm layer, indicating that thicker molecular coatings increase the effective optical path within the hybrid cavity. Although thicker dye layers provide additional spectral tunability, they also broaden the resonance. The linewidth increases from 2.87 nm to 6.53 nm, while the resonance contrast decreases from 0.62 to 0.31. Consequently, the FOM decreases from approximately 40 RIU^{-1} to 18 RIU^{-1}. These results indicate that excessive dye thickness weakens the spectral selectivity of the Fano resonance. For the present design, tdye = 30 nm provides the best compromise between resonance sharpness, spectral contrast, and sensing performance. The dye layer thickness controls the spatial overlap between the plasmonic near field and the excitonic polarization. A thin layer provides insufficient interaction volume, whereas an excessively thick layer extends beyond the decay length of the evanescent plasmonic field. Therefore, an intermediate thickness maximizes plasmon–exciton coupling strength and produces the strongest hybrid Fano resonance. A comprehensive summary of the calculated wavelength-

shift sensing metrics for all investigated refractive-index values is presented in Table S5 of the Supplementary Information.

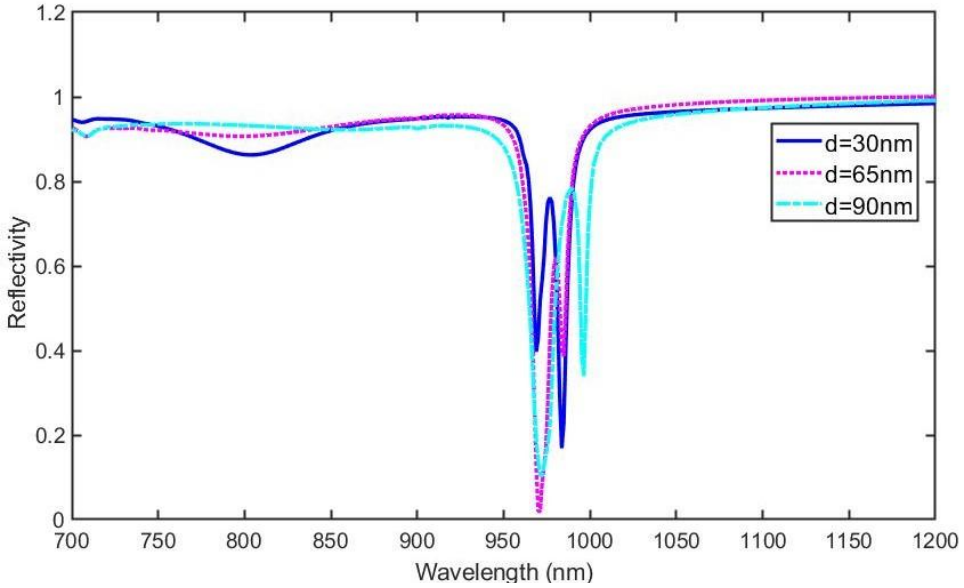


Fig. 9. Reflection spectra of the nanostructure for different excitonic dye-layer thicknesses (t_{dye}=30, 65, and 90 nm) at a fixed lattice period of 600 nm. Increasing the dye thickness induces a systematic redshift of the central resonance peak and suppresses secondary features, indicating stronger optical-path accumulation and increased damping of the coupled Fano mode.

3.4.2. Effect of Lattice Periodicity

The lattice period determines the collective optical response of the nanorod array by controlling the diffractive interaction between neighboring nanorods. Reflection spectra were calculated for lattice periods of 580, 600, and 620 nm, and the resonance wavelength was monitored over the refractive-index range 1.50–1.56. As illustrated in Fig. 10, increasing the lattice period results in a systematic redshift of the hybrid resonance together with a significant increase in refractive-index sensitivity.

The extracted sensitivities are summarized in Table S3. The wavelength sensitivity increases from 38.15 nm/RIU for p = 580 nm to 57.10 nm/RIU for 600 nm, reaching 114.95 nm/RIU for 620 nm. The larger periodicity provides more favorable coupling between the localized plasmon resonance and the collective lattice response, thereby increasing the sensitivity of the hybrid resonance to dielectric perturbations. Among the investigated geometries, p = 620 nm provides the highest wavelength sensitivity and the largest FOM, and was therefore selected as the optimum lattice configuration. The lattice period p governs the diffractive coupling between neighboring nanorods and the formation of collective lattice modes. Reflection spectra were evaluated for p=580, 600, and 620 nm over the refractive-index range n=1.50 to 1.56. The lattice period determines the phase relationship between neighboring nanorods and therefore controls lattice-assisted optical coupling. As the period approaches the condition for constructive diffractive interaction, collective lattice modes increase the coherence of the hybrid resonance and reduce radiative broadening. Excessively large periods weaken inter-particle coupling, whereas smaller periods introduce

stronger near-field interactions and increased damping. The resonance wavelengths were extracted from the Fano dip, and the sensitivity was determined from the slope of linear regression of λ_{res} versus n. The numerical data used to evaluate the intensity-based sensing performance, including the calculated intensity ratios and corresponding sensitivities, are summarized in Table S6 of the Supplementary Information.

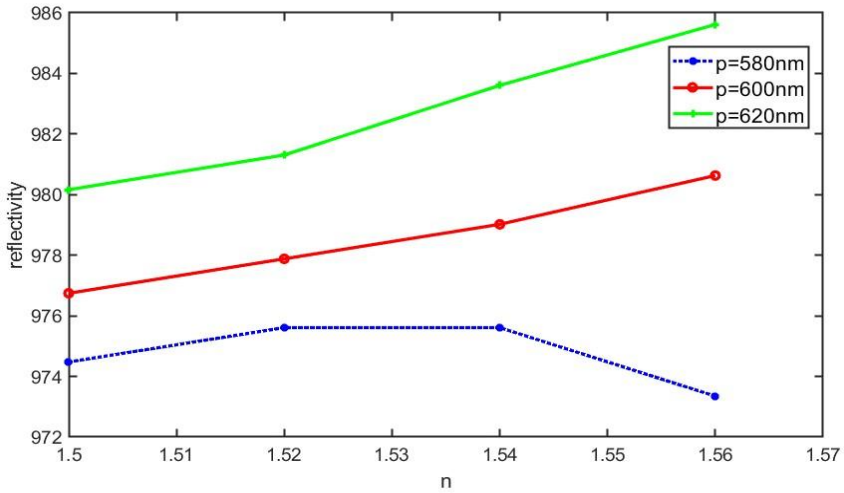


Fig. 10. Dependence of the resonance wavelength on lattice periodicity for the periodic Au nanorod–dye structure. Results are shown for p=580, 600, and 620 nm over the refractive-index range n=1.50–1.56. Increasing the period produces a clear redshift of the resonance and modifies the wavelength-shift sensitivity, confirming that lattice periodicity is an effective tuning parameter for optimizing refractive-index sensing.

3.4.3. Comparison with Multilayer Ellipsoidal Configuration

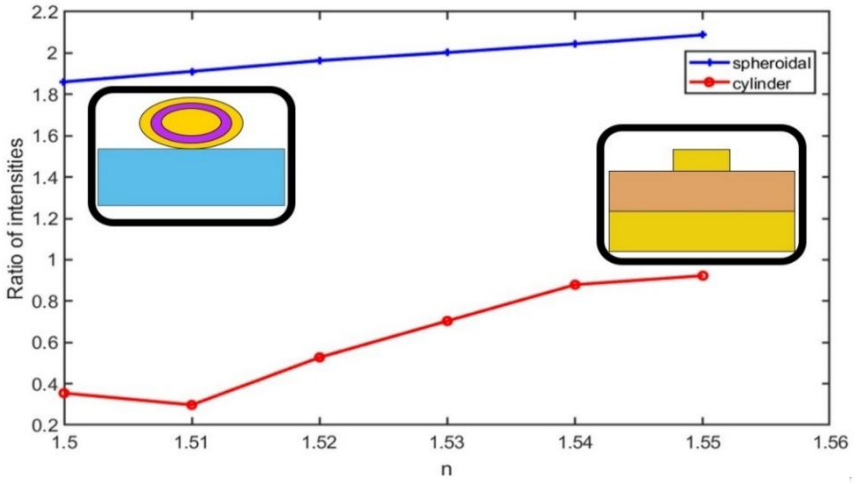
To assess the benefits of the proposed nanorod geometry, its sensing performance was compared with that of a multilayer ellipsoidal plasmonic structure simulated under identical numerical conditions [12,13,55]. As summarized in Tables 4 and 5 and illustrated in Fig. 11, the nanorod array consistently outperforms the ellipsoidal configuration in both wavelength-based and intensity-based sensing.

For the refractive-index range 1.50–1.56, the wavelength sensitivity increases from 83.42 nm/RIU for the ellipsoid to 114.95 nm/RIU for the nanorod array. Within the biomaterial range (1.46–1.55), the selected nanorod structure reaches 333.93 nm/RIU, representing an improvement of approximately 55% over the reference configuration. Similarly, the intensity sensitivity increases from 0.45 RIU^{-1} to 2.07 RIU^{-1}, demonstrating the superior modulation capability of the proposed architecture. The improved performance can be attributed to the larger active surface area, stronger electromagnetic confinement, and the collective optical response supported by the periodic nanorod array.

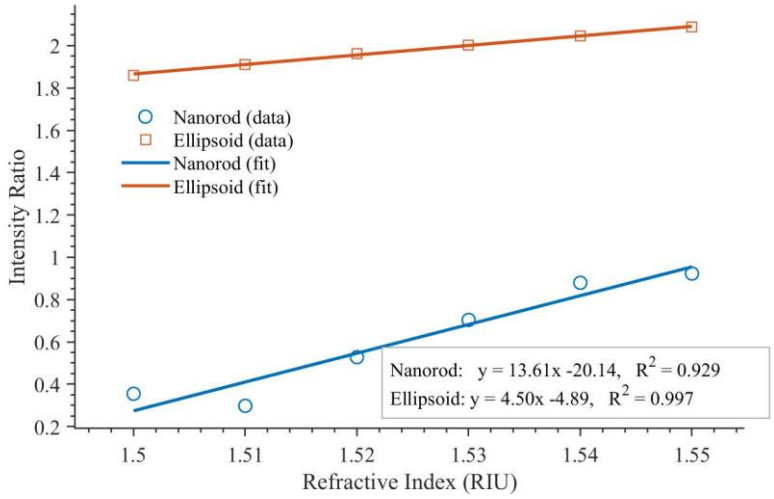
Table 4. Wavelength-shift sensitivity comparison between nanorod array and multilayer ellipsoid.

Structure	**Refractive-Index Range**	S_λ**(nm/RIU)**	R^2
Nanorod Array	1.50–1.56	114.95	0.987

Nanorod Array	1.46–1.55	333.926	0.991
Multilayer Ellipsoid	1.50–1.56	83.42	0.985
Multilayer Ellipsoid	1.46–1.55	215.7	0.989



(a)



(b)

Fig. 11. Comparative sensing performance of the nanorod array and the multilayer ellipsoid configurations. (a) Wavelength-shift sensitivity S_λ extracted from the resonance wavelength versus refractive index; the nanorod geometry shows consistently larger sensitivity. (b) Intensity-based response quantified by the ratio $R=I_{peak}/I_{dip}$ as a function of refractive index; the steeper linear slope for the nanorod structure indicates stronger intensity modulation for small refractive-index changes.

3.4.4. Broad-Range Sensing Performance

Having established the underlying resonance-engineering mechanism, the proposed hybrid platform was evaluated over refractive-index ranges representative of practical sensing applications. Figure 12 summarizes the wavelength-interrogation performance for the different refractive-index regimes.

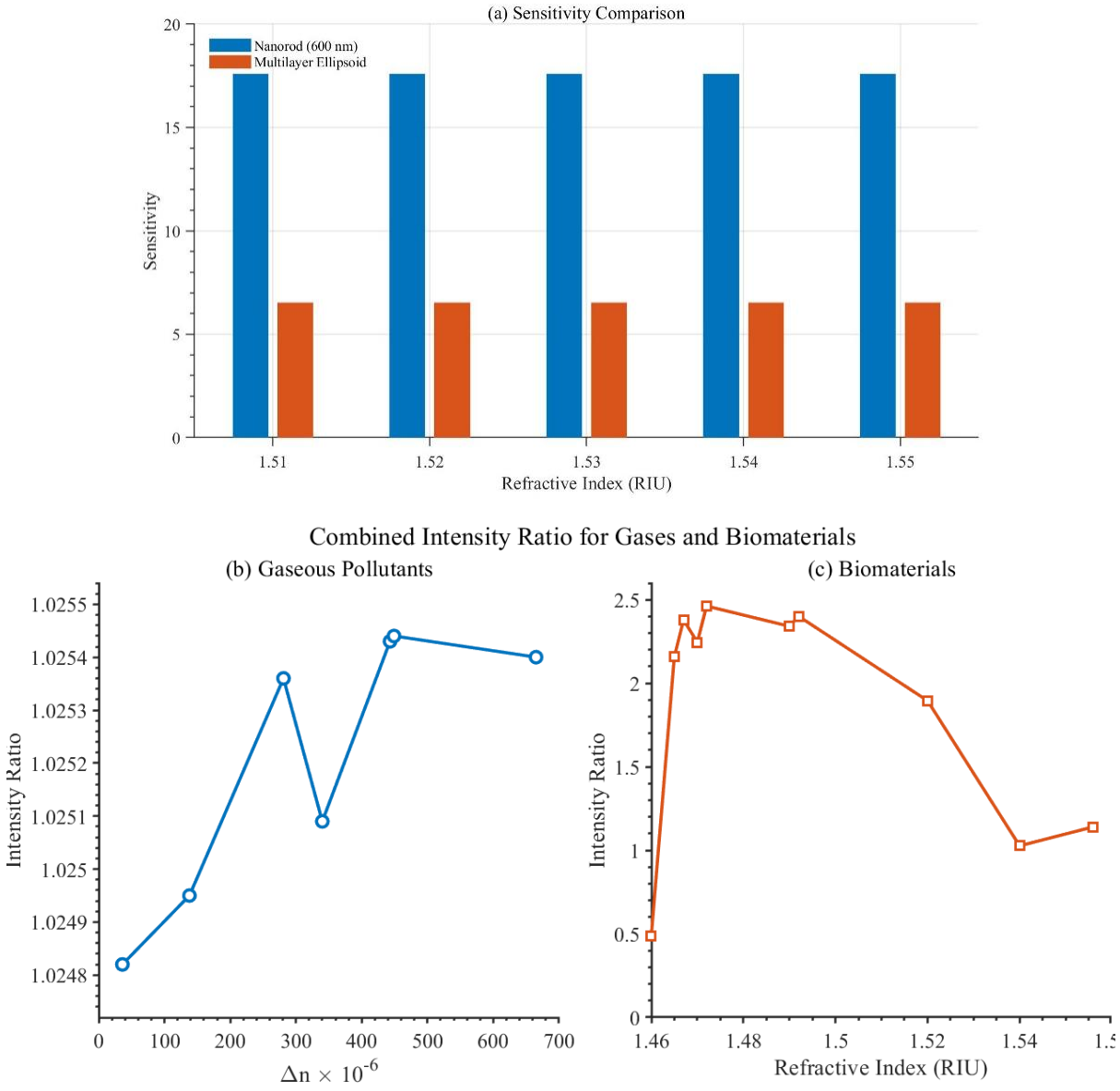


Fig. 12. Sensing performance summary for the hybrid structure (p=600 nm): (a) Wavelength-shift sensitivity S_λ; (b) Resonance response in representative low and high refractive-index environments.

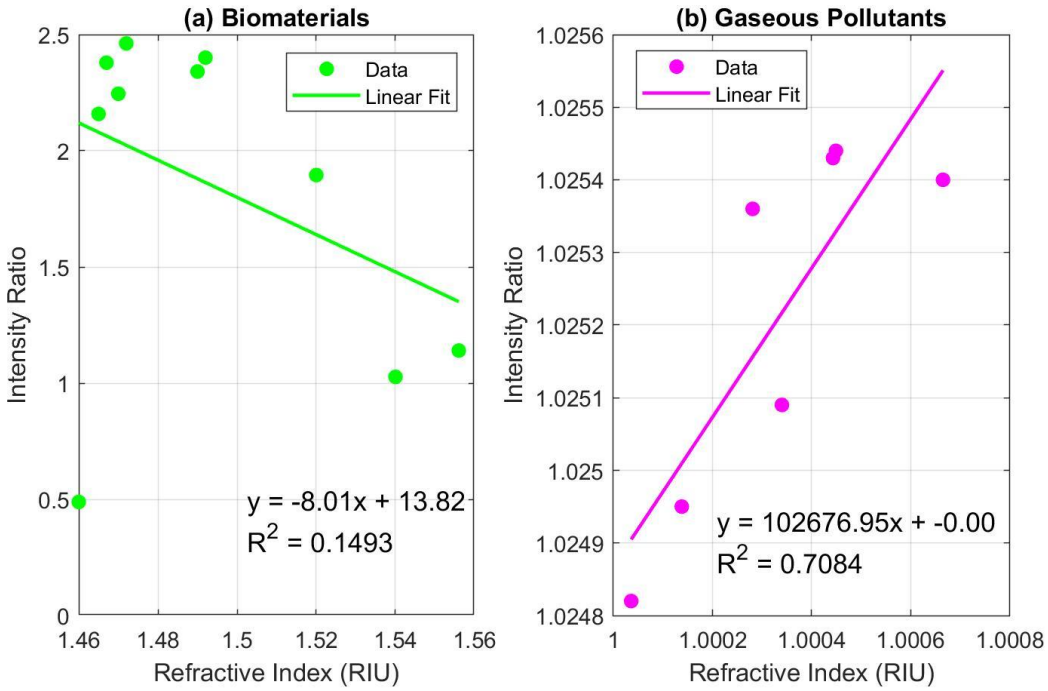


Fig. 13. Linear regression of the intensity-ratio response R versus refractive index for (a) biomaterial-range indices and (b) gaseous-pollutant-range indices. The fitted slopes quantify the intensity-based sensitivity S_I. A larger slope indicates stronger intensity modulation per refractive-index change and is advantageous for fixed-wavelength detection schemes.

For biological media (n = 1.46–1.55), wavelength interrogation provides the highest performance, yielding a sensitivity of 333.93 nm/RIU with an estimated detection limit of approximately 3×10^{-5} RIU. In this higher refractive-index regime, a larger fraction of the evanescent field penetrates the surrounding dielectric, increasing the perturbation experienced by the hybrid optical mode. Consequently, the resonance wavelength becomes more responsive to refractive-index variations. In contrast, for gaseous analytes with refractive indices close to unity, the induced wavelength shifts become extremely small and may approach the spectral resolution limit of practical spectrometers. Under these conditions, fixed-wavelength intensity interrogation offers a more practical sensing strategy by exploiting the steep slope of the Fano resonance to convert minute spectral shifts into readily measurable intensity variations. The highest-performing structure exhibits an intensity sensitivity of 17.58 RIU^{-1}, with excellent linearity ($R^2 = 0.988$), making the platform suitable for detecting small refractive-index variations in low-index environments. The corresponding linear relationships between the intensity ratio and refractive index for both biomaterial and gaseous sensing regimes are shown in Fig. 13, from which the intensity sensitivities were obtained by linear regression. A summary of the sensing performance achieved using the two interrogation schemes is provided in Table 6. Overall, these results demonstrate that the proposed hybrid nanorod–dye architecture provides a versatile sensing platform capable of supporting both wavelength-shift and intensity-based interrogation, depending on the target refractive-index range.

Table 5 compares the proposed sensor with representative plasmonic refractive-index sensing platforms reported in the literature. In addition to wavelength sensitivity, the comparison highlights the underlying resonance mechanism, emphasizing that the present architecture employs cooperative plasmon–exciton, lattice, and cavity interactions rather than relying on a single plasmonic resonance.

Table 5. Comparison of refractive-index sensitivity for various plasmonic and hybrid nanostructures.

Structure	***Resonance Type***	***Coupling Mechanism***	***Sensitivity (nm/RIU)***	***FOM***	***Remarks***
Nanorod–Dye Hybrid (This work)	**Plasmon–exciton + lattice + Fabry–Pérot coupling**	**Hybrid Fano**	**333.926**	**1.46–1.55**	**Cooperative resonance-engineering framework**
Au nanorods [61]	Localized plasmon resonance	LSPR	~200–300	–	Distance-dependent RI sensing
Conventional Au nanorods [60]	Localized plasmon resonance	LSPR	200–366	–	Single plasmonic mode
Au–Ag core–shell nanorods [62]	Localized plasmon + Ag shell	LSPR	~300–400	Improved over bare AuNR	Geometry-assisted enhancement
MIM waveguide [64]	Waveguide–cavity coupling	Fano	926	135	Comparative study of Au nanostructures
Gaseous Sensing (This work)	**Hybrid plasmon–exciton resonance**	**Hybrid Fano (Intensity)**	**17.58 (RIU^{-1})**	**~1.000–1.001**	**Cooperative resonance-engineering framework**
AuNR@Pd [7]	Subradiant–superradiant plasmon coupling	Fano resonance	RI-dependent	–	Single-particle Fano sensing
Hybrid plasmonic sensors [65]	Coupled plasmonic modes	Hybrid/Fano	Various	Various	Review of hybrid plasmonic sensing

As summarized in Table 5, the proposed hybrid architecture employs a fundamentally different resonance-engineering strategy from that of conventional plasmonic refractive-index sensors. Many reported designs improve sensing performance primarily through geometric tuning of localized plasmonic resonances. In contrast, the present structure intentionally combines plasmon–exciton coupling, lattice-assisted optical confinement, and Fabry–Pérot cavity feedback to engineer a narrow hybrid Fano resonance. The cooperative interaction of these mechanisms suppresses radiative losses, strengthens electromagnetic field localization, and enhances spectral selectivity, leading to a higher quality factor, narrower resonance linewidth, and improved figure of merit. These findings indicate that the enhanced sensing performance originates from cooperative mode hybridization rather than geometric parameter tuning alone. More broadly, the proposed resonance-engineering framework provides general physical design principles that may be extended to other hybrid plasmonic materials, resonator geometries, and integrated photonic sensing platforms.

The proposed hybrid structure exhibits higher refractive-index sensitivity than conventional Au nanorod sensors (200–250 nm/RIU) and Au nanoshell biosensors (~280 nm/RIU). This enhancement stems from the Fano-like resonance providing sharper spectral features, collective lattice resonances reducing radiative damping, and the cylindrical nanorod geometry providing stronger field localization and larger surface area for analyte interaction.

Table 6. Summary of performance comparison between wavelength and intensity interrogation

Metric	Wavelength-based sensing	Intensity-based sensing
Refractive-index range	1.46–1.55	1.000–1.001
Measured parameter	λ_{res}	Peak/Dip ratio
Sensitivity	333.93 nm RIU^{-1}	17.58 RIU^{-1}
Figure of Merit	116.35 RIU^{-1}	—
Detection Limit	3.0×10^{-5} RIU	-
Resonance linewidth	2.87 nm	Same resonance
Quality factor	343	Same resonance
Contrast ratio	0.89	0.89
Electromagnetic enhancement	746	746
Confinement factor Γ	0.63	0.63
Recommended application	Biomolecular sensing	Gas sensing

3.5. Practical Considerations and Design Guidelines

The numerical results presented in the previous sections demonstrate that the proposed Au nanorod–dye hybrid architecture provides a flexible sensing platform capable of operating over a wide refractive-index range. Depending on the target application, either wavelength-shift interrogation or fixed-wavelength intensity monitoring may be employed. From the structural optimization performed in Sections 3.3 and 3.4, three design considerations emerge. First, relatively short nanorods ($h \approx 25$ nm) provide the highest resonance quality by maintaining strong electromagnetic confinement while minimizing radiative broadening. Second, a moderate

molecular dye thickness ($t_{dye} \approx 30$ nm) achieves the best balance between plasmon–exciton interaction and resonance linewidth. Increasing the dye thickness shifts the resonance to longer wavelengths but simultaneously broadens the spectral response and reduces the FOM. Third, increasing the lattice period enhances the refractive-index sensitivity through improved collective optical response, with p = 620 nm providing the optimum performance among the investigated geometries. These design guidelines provide practical parameters for fabrication using standard nanolithography together with spin-coating or layer-by-layer deposition of the molecular film. Because the highest-performing dimensions are compatible with existing plasmonic fabrication techniques, experimental realization of the proposed architecture should be feasible. Although the present study is based on three-dimensional FDTD simulations, several factors should be considered before practical implementation. Fabrication imperfections, surface roughness, nanorod size dispersion, and molecular-film inhomogeneity may broaden the resonance linewidth and slightly reduce the achievable sensitivity. Furthermore, temperature-dependent variations in the refractive index of both the analyte and the molecular layer may influence the resonance position under experimental conditions.

Future work should therefore focus on experimental validation of the proposed platform together with investigation of molecular adsorption kinetics, fabrication tolerances, and multiplexed sensing using functionalized molecular coatings. Such studies would further clarify the applicability of hybrid plasmon–exciton resonances for chemical and biological sensing. Overall, the highest-performing nanorod–dye architecture combines narrow Fano resonances, strong electromagnetic confinement, and tunable structural parameters to provide a versatile platform for high-resolution refractive-index sensing across both biological and gaseous environments [48][53].

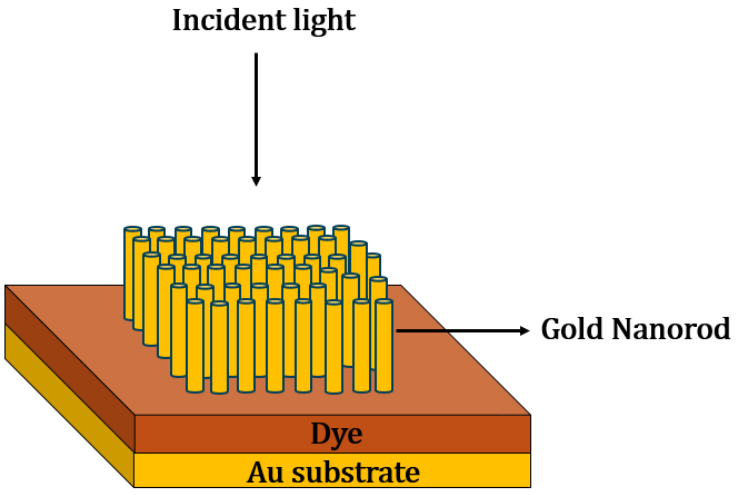


Fig. 14. Conceptual schematic of the LoC-integrated Au nanorod–dye sensor for microfluidic applications.

Compared with previously reported plasmonic refractive-index sensors, the proposed architecture provides advances beyond incremental improvements in sensitivity. Many conventional plasmonic

sensors rely predominantly on geometric tuning of one dominant resonance mechanism, such as localized surface plasmon resonances, cavity resonances, or isolated Fano resonances. In contrast, the present design intentionally engineers a hybrid Fano resonance through the cooperative interaction of localized surface plasmons, molecular excitons, lattice-assisted optical confinement, and Fabry–Pérot cavity feedback within a periodic nanorod array. The interplay of these mechanisms simultaneously suppresses radiative losses, strengthens electromagnetic field localization, and improves spectral selectivity, leading to narrower resonances, higher quality factors, and enhanced refractive-index sensing performance. More importantly, the results demonstrate that the observed performance originates from cooperative mode hybridization rather than geometric parameter tuning alone. Consequently, this work establishes a general resonance-engineering framework that can be extended to other hybrid plasmonic materials, resonator geometries, and integrated photonic sensing platforms.

To illustrate the practical applicability of the proposed sensing concept, a conceptual implementation integrated with a lab-on-a-chip (LoC) microfluidic platform is presented in Fig. 14. The schematic highlights the compatibility of the periodic Au nanorod–dye architecture with continuous analyte delivery and compact optical readout, demonstrating its potential for future integrated sensing systems[56-59]. It should be emphasized that this figure represents a prospective implementation intended to illustrate the application of the proposed design rather than an experimentally realized device. Overall, the physical design principles established in this work provide practical guidelines for developing compact, label-free hybrid plasmonic sensors for biochemical, environmental, and integrated photonic sensing applications.

3.6. Limitations and Simulation Accuracy Considerations

The sensing performance reported in this study represents the theoretical response of the proposed nanorod–dye hybrid architecture under idealized conditions. Several factors associated with the material models, numerical implementation, and fabrication tolerances should be considered when interpreting the predicted performance. The optical properties of gold were described using the Drude model, which accurately reproduces the free-electron response in the near-infrared spectral range (960–1000 nm) where the hybrid Fano resonance is located. Although this approximation neglects interband transitions at shorter wavelengths, their influence on the primary resonance is expected to be minimal. The molecular dye layer was modeled using a single Lorentz oscillator with homogeneous broadening. In practice, molecular disorder, aggregation, and multiple excitonic transitions may broaden the resonance and reduce the achievable sensitivity. Future studies could employ Drude–Lorentz dielectric models together with experimentally measured optical constants to improve the quantitative accuracy of the simulations.

The numerical convergence of the 3D-FDTD calculations was verified using a non-uniform conformal mesh. The complete mesh-convergence results used to verify the numerical stability of the simulations are listed in Table S7 of the Supplementary Information, confirming that the selected computational mesh provides converged resonance characteristics. Additional quantitative results of the fabrication tolerance analysis are provided in Table S8 of the Supplementary Information, illustrating the influence of realistic dimensional variations on the

resonance wavelength, linewidth, and sensing performance. As summarized in Table S9 , reducing the minimum mesh size from 6 nm to 3 nm changed the resonance wavelength by less than 0.05 nm and the linewidth by less than 1.5%, confirming that the selected mesh provides sufficient numerical accuracy. Similarly, increasing the thickness of the PML or reducing its reflection coefficient produced negligible changes in the calculated spectra. In practical implementations, fabrication imperfections are expected to be the primary source of performance degradation. Variations in nanorod dimensions, lattice periodicity, dye-layer thickness, surface roughness, and coating uniformity can shift the resonance wavelength, broaden the linewidth, and reduce field localization. The tolerance analysis summarized in Table S10 indicates that the nanorod dimensions are the most critical parameters, where dimensional variations of approximately ±2 nm may reduce the wavelength sensitivity by 8–10% while increasing the linewidth by up to 15%. These effects can be mitigated through high-resolution nanofabrication techniques such as electron-beam lithography and conformal thin-film deposition. The predicted sensing performance therefore represents an upper theoretical limit. Experimental factors including surface roughness, molecular inhomogeneity, photobleaching, temperature fluctuations, and measurement noise are expected to reduce the achievable FOM under practical operating conditions. Nevertheless, the simulations establish realistic performance trends and identify the structural parameters that most strongly influence the hybrid resonance.

Future work should focus on experimental validation of the proposed architecture, fabrication-tolerance analysis using statistical approaches such as Monte Carlo simulations, and implementation of selective surface functionalization for chemical and biological sensing. These investigations will further assess the robustness of the proposed design and facilitate its integration into practical plasmonic sensing platforms.

4. Conclusion

This study presented a hybrid plasmon–exciton sensing platform based on a periodic array of gold nanorods conformally coated with a molecular dye layer and investigated its optical response using 3D-FDTD simulations. The results indicate that the narrow Fano resonance originates from the interplay between localized plasmonic modes and the excitonic response of the dye layer, while collective lattice effects and cavity-assisted feedback further improve spectral confinement. A systematic parametric study identified a nanorod height of 25 nm, a dye-layer thickness of 30 nm, and a lattice period of 620 nm as the preferred design configuration, providing an effective balance between resonance linewidth and sensing performance. Under these conditions, the proposed platform achieved a maximum wavelength sensitivity of 333.93 RIU^{-1} nm, a FOM of 116.35 RIU^{-1}, and an estimated detection limit of 3.0×10^{-5} RIU for biomaterial sensing. For low-index gaseous analytes, where spectral shifts are intrinsically small, the same structure also supports fixed-wavelength intensity interrogation with an intensity sensitivity of 17.58 RIU^{-1}, demonstrating the versatility of the hybrid platform for different sensing scenarios. The enhanced sensing performance originates from cooperative electromagnetic interactions that simultaneously strengthen field localization while reducing radiative damping.

Beyond the highest-performing sensing performance, this study establishes a general resonance-engineering framework for hybrid plasmonic sensors. The results demonstrate that cooperative plasmon–exciton interaction, lattice-mediated optical confinement, and cavity-enhanced optical feedback collectively govern the formation of narrow Fano resonances, leading to improved field localization, spectral selectivity, and refractive-index sensitivity. These physical design principles are not limited to the specific Au nanorod–dye architecture investigated here and may be extended to other hybrid plasmonic materials and resonator geometries. Although the present study is based on numerical simulations under idealized conditions, the proposed design is compatible with established nanofabrication techniques and microfluidic integration, providing a practical foundation for future experimental realization. Further work should focus on fabrication tolerance analysis, experimental validation, and surface functionalization for selective biochemical and environmental sensing applications.

Acknowledgments

The authors gratefully acknowledge financial support from the Research Council of Persian Gulf University.

Declarations

Credit authorship contribution statement

Maedeh Sadeghzadeh: Methodology, Formal analysis, Writing – original draft, Writing – review & editing, Visualization, Investigation. Ahmad Mohammadi: Supervision, Visualization, Conceptualization, Methodology, Validation, review & editing. Tahmineh Jalali: Writing – review & editing, Conceptualization, Investigation.

Funding

Not applicable

Conflict of Interest

The authors declare that they have no conflict of interest.

Ethical approval

This paper does not contain any studies with human participants or animals performed by any of the authors.

Declaration of Generative AI and AI-assisted technologies

All text, figures, and tables were created by the author without the assistance of AI. The authors used a generative AI tool solely to improve the language, grammar, and clarity of the manuscript.

Consent to participate

Not applicable

Consent for publication

Not applicable

Availability of data and material

The data supporting this study's findings are available from the corresponding author.

Code Availability

The code supporting this study's findings is available from the corresponding author.

References

1. Minamiki, T., et al., *Accurate and reproducible detection of proteins in water using an extended-gate type organic transistor biosensor.* Applied Physics Letters, 2014. **104**(24): p. 243703.
2. Matsui, J., et al., *SPR sensor chip for detection of small molecules using molecularly imprinted polymer with embedded gold nanoparticles.* Analytical Chemistry, 2005. **77**(13): p. 4282–4285.
3. Liang, W., et al., *Highly sensitive fiber Bragg grating refractive index sensors.* Applied physics letters, 2005. **86**(15): p. 151122.
4. Velázquez-González, J.S., et al., *Simultaneous measurement of refractive index and temperature using a SPR-based fiber optic sensor.* Sensors and Actuators B: Chemical, 2017. **242**: p. 912–920.
5. Sadkovskyi, R., T. Bulavinets, and I. Yaremchuk. *Surface Plasmon Enhanced Copper Monosulfide-Based Core–Shell Nanoparticles*. in *Nanooptics and Photonics, Nanochemistry and Nanobiotechnology, and Their Applications: Selected Proceedings of the IX International Conference Nanotechnology and Nanomaterials (NANO2021), 25–28 August 2021, Lviv, Ukraine*. 2023. Springer.
6. Sadeghi, Z., N. Shojaeihagh, and H. Shirkani, *Multiple-step graphene grating optical sensors based on surface plasmons in IR range for ultra-sensing biomolecules.* Materials Science and Engineering: B, 2021. **265**: p. 114988.
7. Firmanti, Metya Indah, and Ji Won Ha. *Elucidating refractive index sensitivity on subradiant, superradiant, and fano resonance modes in single palladium-coated gold nanorods.* Scientific Reports: 2024, **14**, 1: p. 20182.
8. Jarahizadeh, Y., et al., *Designing a Perfect Surface Plasmon Resonance Absorber Based on Graphene and Hexagonal Boron Nitride Photonic Crystal Nanorods.* SSRN 4367516.
9. Firoozi, A., et al., *Plasmon-exciton interactions in a spheroidal multilayer nanoshell for refractive index sensor application.* The European Physical Journal Plus, 2021. **136**: p. 1–15.
10. Choi, J.H., et al., *Graphene-based gas sensors with high sensitivity and minimal sensor-to-sensor variation.* ACS Applied Nano Materials, 2020. **3**(3): p. 2257–2265.
11. Jalali, T., *MMP simulation of coupled gold nanoparticles as nanoantennae: Efficient tuning of localized surface plasmon resonances.* Journal of Quantitative Spectroscopy and Radiative Transfer, 2023. **311**: p. 108786.
12. Firoozi, A., et al., *Effect of nanoshell geometries, sizes, and quantum emitter parameters on the sensitivity of plasmon-exciton hybrid nanoshells for sensing application.* Scientific Reports, 2023. **13**(1): p. 11325.
13. Firoozi, A., A. Mohammadi, and T. Jalali, *Maxwell–Bloch FDTD study of plasmon–exciton coupling in geometry-optimized nanoshells for refractive index sensing.* Optical and Quantum Electronics, 2025. **57**(10): p. 544.
14. Islam, M.S., et al., *Localized surface plasmon resonance biosensor: an improved technique for SERS response intensification.* Optics letters, 2019. **44**(5): p. 1134–1137.
15. Qu, B., et al., *Surface plasmon resonance intensification by cavity-ring plasma structure in the giga-hertz regime.* Plasmonics, 2020. **15**: p. 1591–1597.
16. Choi, Y.M., et al., *Intensified near-field by localizing surface plasmon for enhancing photoelectrochemical responses via periodically patterned Au assemblies.* Chemical Engineering Journal, 2023. **461**: p. 142082.
17. Kasani, S., K. Curtin, and N. Wu, *A review of 2D and 3D plasmonic nanostructure array patterns: fabrication, light management and sensing applications.* Nanophotonics, 2019. **8**(12): p. 2065–2089.
18. Bao, Y., & Oluwafemi, A. *Recent advances in surface modified gold nanorods and their improved sensing performance.* Chemical Communications, 2024. **60**(5): p. 469-481.
19. Li, M., et al., *High-Q Fano resonance in subwavelength stub-wall-coupled MDM waveguide structure and its terahertz sensing application.* IEEE Access, 2021. **9**: p. 123939–123949.
20. Willner, I. and E. Katz, *Bioelectronics: from theory to applications*. 2006: John Wiley & Sons.

21. Fleming, W.J., D.S. Howarth, and D.S. Eddy, *Sensor for on-vehicle detection of engine exhaust gas composition.* SAE Transactions, 1973: p. 1969–1984.
22. Wolfbeis, O.S., *Fiber-optic chemical sensors and biosensors.* Analytical chemistry, 2006. **78**(12): p. 3859–3874.
23. Brecht, A. and G. Gauglitz, *Optical probes and transducers.* Biosensors and Bioelectronics, 1995. **10**(9-10): p. 923–936.
24. Gauglitz, G., *Opto-chemical and opto-immuno sensors.* Sensors update, 1996. **1**(1): p. 1–48.
25. Esfahani Monfared, Y., *Refractive index sensor based on surface plasmon resonance excitation in a D-shaped photonic crystal fiber coated by titanium nitride.* Plasmonics, 2020. **15**(2): p. 535–542.
26. Nasirifar, R., M. Danaie, and A. Dideban, *Hollow-core graded index optical fiber refractive index sensor based on surface plasmon resonance.* Optical and Quantum Electronics, 2020. **52**: p. 1–23.
27. Farmani, A. and A. Mir, *Graphene sensor based on surface plasmon resonance for optical scanning.* IEEE Photonics Technology Letters, 2019. **31**(8): p. 643–646.
28. Loiseau, A., et al., *Silver-based plasmonic nanoparticles for and their use in biosensing.* Biosensors, 2019. **9**(2): p. 78.
29. Unser, S., et al., *Localized surface plasmon resonance biosensing: current challenges and approaches.* Sensors, 2015. **15**(7): p. 15684–15716.
30. Hao, X., & Qin, J. *Recent Advances and Synthetic Approaches of AuNRs for Sensing Applications Based on Different Aspect Ratios*. Advanced Sensor Research, 2024. **3**(7), p. 2300192.
31. Maier, S.A., *Plasmonics: fundamentals and applications*. Vol. 1. 2007: Springer.
32. Sepúlveda, B., et al., *LSPR-based nanobiosensors.* Nano today, 2009. **4**(3): p. 244–251.
33. Chen, G., et al., *Nanochemistry and nanomedicine for nanoparticle-based diagnostics and therapy.* Chemical reviews, 2016. **116**(5): p. 2826–2885.
34. Masson, J.-F., *Portable and field-deployed surface plasmon resonance and plasmonic sensors.* Analyst, 2020. **145**(11): p. 3776–3800.
35. Rabbani, M., M.E. Hoque, and Z.B. Mahbub, *Nanosensors in biomedical and environmental applications: Perspectives and prospects.* Nanofabrication for smart nanosensor applications, 2020: p. 163–186.
36. Ravindran, N., et al., *Recent advances in Surface Plasmon Resonance (SPR) biosensors for food analysis: A review.* Critical Reviews in Food Science and Nutrition, 2023. **63**(8): p. 1055–1077.
37. Philip, A. and A.R. Kumar, *The performance enhancement of surface plasmon resonance optical sensors using nanomaterials: A review.* Coordination Chemistry Reviews, 2022. **458**: p. 214424.
38. Singh, G.P. and N. Sardana, *Smartphone-based surface plasmon resonance sensors: a review.* Plasmonics, 2022. **17**(5): p. 1869–1888.
39. Zhou, X.L., et al., *Surface plasmon resonance microscopy: From single-molecule sensing to single-cell imaging.* Angewandte Chemie International Edition, 2020. **59**(5): p. 1776–1785.
40. Xu, Y., et al., *Optical refractive index sensors with plasmonic and photonic structures: promising and inconvenient truth.* Advanced Optical Materials, 2019. **7**(9): p. 1801433.
41. Tan, P., et al., *Silver nanoparticle in biosensor and bioimaging: Clinical perspectives.* Biotechnology and Applied Biochemistry, 2021. **68**(6): p. 1236–1242.
42. Shrivastav, A.M., U. Cvelbar, and I. Abdulhalim, *A comprehensive review on plasmonic-based biosensors used in viral diagnostics.* Communications biology, 2021. **4**(1): p. 70.
43. Saylan, Y., S. Akgönüllü, and A. Denizli, *Plasmonic sensors for monitoring biological and chemical threat agents.* Biosensors, 2020. **10**(10): p. 142.
44. Rahmati, S., et al., *Gold–carbon nanocomposites for environmental contaminant sensing.* Micromachines, 2021. **12**(6): p. 719.
45. Avci, M. B., & Cetin, A. E. *A hybrid plasmonic system integrating plasmon-induced transparency and perfect absorbance*. Plasmonics, 2025: p.1-12.
46. Firoozi, A. and A. Mohammadi, *Design of plasmonic backcontact nanogratings for broadband and polarization-insensitive absorption enhancement in thin-film solar cell.* International Journal of Modern Physics B, 2015. **29**(17): p. 1550111.

47. Chen, K., Guo, H., Huang, T., Zhang, J., Cheng, Z., Lu, M., ... & Shum, P. P. *Ultrasensitive dual Fano resonance sensor based on coupling of plasmonic and multi-order waveguide modes*. Journal of the Optical Society of America B, 2025. **42**(11): p. 2514-2525.
48. Ramola, A., Shakya, A. K., & Bergman, A. *Comprehensive analysis of advancement in optical biosensing techniques for early detection of cancerous cells. Biosensors*, 2025. **15**(5), 292.
49. Xu, X., et al., *Microfluidic devices integrated with plasmonic nanostructures for sensitive fluorescent immunoassays.* Biomicrofluidics, 2024. **18**(1).
50. Mohammadi, A., T. Jalali, and M. Agio, *Dispersive contour-path algorithm for the two-dimensional finite-difference time-domain method.* Optics Express, 2008. **16**(10): p. 7397–7406.
51. Escobedo, C. and A. Brolo, *Synergizing microfluidics and plasmonics: advances, applications, and future directions.* Lab on a Chip, 2025. **25**(5): p. 1256–1281.
52. Jalali, T., et al., *Efficient effective permittivity treatment for the 2D-FDTD simulation of photonic crystals.* Journal of Computational and Theoretical Nanoscience, 2007. **4**(3): p. 644–648.
53. Firoozi, A., et al., *Q-BOR–FDTD method for solving Schrödinger equation for rotationally symmetric nanostructures with hydrogenic impurity.* Physica Scripta, 2022. **97**(2): p. 025802.
54. Lerner, M.B., et al., *Detecting Lyme disease using antibody-functionalized single-walled carbon nanotube transistors.* Biosensors and Bioelectronics, 2013. **45**: p. 163–167. Miroshnichenko, A. E., Flach, S., & Kivshar, Y. S. (2010). Fano resonances in nanoscale structures. Reviews of Modern Physics, 82(3), 2257-2298.
55. Sadeghzadeh, M., A. Mohammadi, and T. Jalali, *FDTD study of plasmon-exciton coupling for bio-nanosensors.* Results in Chemistry, 2025. **16**: p. 102450.
56. Mayer, K.M. and J.H. Hafner, *Localized surface plasmon resonance sensors.* Chemical reviews, 2011. **111**(6): p. 3828–3857.
57. Zhao, B., Jian, A., Li, M., Xue, Y., Wang, K., Li, Y., ... & Sang, S. *Fano resonance sensor based on microhole array waveguides for ultrasensitive label-free biosensing*. ACS sensors, 2025. 10(8), p. 6263-6271.
58. Michaud, M., de l'Escalopier, N., Voisard, C., Oudre, L., & Ricard, D. *Real-world gait study of Parkinson's disease using wearable sensors: a systematic review*. Journal of NeuroEngineering and Rehabilitation. 2026.
59. Kim, B., Youm, C., Cheon, S. M., Park, H., Choi, H., Hwang, J., & Kim, M. *Motor-Derived Digital Biomarkers for Identifying Low-MoCA Status in People with Parkinson's Disease*. *Sensors*, 2026. *26*(8), 2503.
60 . Chen, C.-D., Cheng, S.-F., Chau, L.-K., & Wang, C. R. C. (2007). Sensing capability of the localized surface plasmon resonance of gold nanorods. Biosensors and Bioelectronics, 22(6), 926–932.
61. Mayer, K. M., Lee, S., Liao, H., Rostro, B. C., Fuentes, A., Scully, P. T., Nehl, C. L., & Hafner, J. H. *A label-free immunoassay based upon localized surface plasmon resonance of gold nanorods*. ACS Nano, **2**(4), 2008: p. 687–692.
62. Larsson, E. M., Alegret, J., Käll, M., & Sutherland, D. S. *Sensing characteristics of NIR localized surface plasmon resonances in gold nanorings for application as ultrasensitive biosensors*. Nano Letters, **7**(5), 2007: p. 1256–1263.
63. Marinakos, S. M., Chen, S., & Chilkoti, A. *Plasmonic detection of a model analyte in serum by a gold nanorod sensor*. Analytical Chemistry, **79**(14), 2007: p. 5278–5283.
64. Barbillon, G., Bijeon, J.-L., Plain, J., Royer, P., & Adam, P.-M. *Biological and chemical gold nanosensors based on localized surface plasmon resonance*. Gold Bulletin, **40**(3), 2007: p. 240–244.
65. Singh, L., Balaji, B., Tripathi, Y., Kumar, R., & Yadav, S. *Plasmonic MIM waveguide based FR sensors for refractive index sensing of human hemoglobin.* Photonics and Nanostructures-Fundamentals and Applications, ***62***, 2024: p. 101325.

Supplementary

This supplementary document provides additional numerical data supporting the results presented in the main manuscript. It includes detailed optimization results, analyte properties, mesh-convergence verification, fabrication-tolerance analysis, and supplementary sensing-performance data that complement the discussion in the main text but are not essential for understanding the principal conclusions. The supplementary tables are referenced in the manuscript where appropriate.

Table S1. Refractive index of selected Biomaterials and Gaseous Pollutants

Biomaterials	Refractive index	Gaseous pollutants	Refractive index
Adipose	1.460	Helium	1.000036
Coagulated	1.465	Hydrogen	1.000138
White matter	1.467	Argon	1.000281
Cerebellum	1.470	Carbon monoxide	1.000340
Fat	1.472	Methane	1.000443
Acrylic	1.490	Carbon dioxide	1.000449
Cartilage	1.492	Sulfur dioxide	1.000665
Imaging oil	1.520		
Borosilicate Glass	1.540		
Bone	1.556		

Table S2. Resonance parameters as a function of nanorod height (p=600 nm, t_{dye}=30 nm).

Nanorod Height h(nm)	λ_0(nm)	FWHM (nm)	Quality Factor Q	Contrast Ratio C
25	976.744	2.87	340.3	0.62
50	981.308	4.52	217.1	0.41
75	985.615	7.38	133.6	0.28

Table S3. Resonance wavelengths and wavelength-shift sensitivity of the nanorod array for different lattice periodicities (h=25 nm, t_{dye}=30 nm).

p(nm)	N	λ_{res}(nm)	S_λ (nm/RIU)	R^2
580	1.50	974.478	38.15	0.892

580	1.52	975.610		
580	1.54	976.744		
580	1.56	977.881		
600	1.50	976.744	57.10	0.999
600	1.52	977.881		
600	1.54	979.021		
600	1.56	980.163		
620	1.50	980.163	114.95	0.987
620	1.52	981.308		
620	1.54	983.607		
620	1.56	985.615		

Table S4. Intensity-based sensing performance comparison.

Structure	**Refractive-Index Range**	S_I **(RIU^{-1})**	R^2
Nanorod Array	1.50–1.55	2.07	0.987
Multilayer Ellipsoid	1.50–1.55	0.45	0.993

Table S5. Refractive-index range for target analytes.

Refractive-Index Range	Target Analytes	Sensing Modality
1.000–1.001	Gaseous pollutants (He, H_2, CO, CH_4, CO_2, SO_2)	Intensity-based
1.46–1.55	Biomaterials (adipose, tissue, bone, imaging oil, glass)	Wavelength-shift

Table S6. Intensity ratios and sensitivity for gaseous pollutant detection (p=600 nm, h=25 nm, t_{dye}=30 nm).

Refractive Index	Intensity Ratio R	Sensitivity S_I (RIU^{-1})	R^2
1.500	0.3545	17.58	0.988
1.510	0.2975		
1.520	0.5275		
1.530	0.7037		
1.540	0.8791		
1.550	0.9228		

Table S7. Intensity ratio response for gaseous pollutant detection (p=600 nm, h=25 nm, t_{dye}=30 nm).

Analyte	Refractive Index	Intensity Ratio RR	Relative Change (%)
Helium	1.000036	0.9853	—
Hydrogen	1.000138	0.9791	0.63
Argon	1.000281	0.9702	1.54
Carbon Monoxide	1.000340	0.9658	1.98
Methane	1.000443	0.9553	3.05
Carbon Dioxide	1.000449	0.9547	3.11
Sulfur Dioxide	1.000665	0.9274	5.88

Table S8. Wavelength-shift sensitivity for representative biomaterials (p=600 nm, h=25 nm, t_{dye}=30 nm).

Biomaterial	Refractive Index	Resonance Wavelength (nm)	S_λ (nm/RIU)
Adipose Tissue	1.460	963.81	333.926
Coagulated Tissue	1.465	965.48	333.926
White Matter	1.467	966.15	333.926
Cerebellum	1.470	967.15	333.926
Fat	1.472	967.82	333.926
Acrylic	1.490	973.83	333.926
Cartilage	1.492	974.50	333.926
Imaging Oil	1.520	983.61	333.926
Borosilicate Glass	1.540	990.29	333.926
Bone	1.556	995.63	333.926

Table S9. Mesh convergence study for p=600 nm, h=25 nm, t_{dye}=30 nm.

Minimum Mesh Size (nm)	λ_0 (nm)	FWHM (nm)	Q-Factor
6	983.607	2.87	342.7
4	983.562	2.84	346.3
3	983.528	2.83	347.5

Table S10. Tolerance analysis for key fabrication parameters.

Parameter	Nominal Value	Variation	Effect on λ_0	Effect on FWHM	Effect on S_λ
Nanorod Height	25 nm	±2 nm	±1.8 nm	+12%	−8%

Parameter	Nominal Value	Variation	Effect on λ_0	Effect on FWHM	Effect on S_λ
Nanorod Diameter	20 nm	±2 nm	±2.3 nm	+15%	−10%
Dye-Layer Thickness	30 nm	±3 nm	±1.2 nm	+8%	−5%
Lattice Period	600 nm	±5 nm	±0.8 nm	+3%	−3%